ADVANCED FUNCTIONAL MATERIALS
www.afm-journal.de

www.MaterialsViews.com

Ultrahigh-Performance Pseudocapacitor Electrodes Based on Transition Metal Phosphide Nanosheets Array via Phosphorization: A General and Effective Approach

Kai Zhou, Weijia Zhou, Linjing Yang, Jia Lu, Shuang Cheng, Wenjie Mai, Zhenghua Tang, Ligui Li, and Shaowei Chen**

In this study, a general and effective phosphorization strategy is successfully demonstrated to enhance supercapacitor performance of various transition metals oxide or hydroxide, such as $Ni(OH)_2$, $Co(OH)_2$, MnO_2, and Fe_2O_3. For example, a 3D networked Ni_2P nanosheets array via a facile phosphorization reaction of $Ni(OH)_2$ nanosheets is grown on the surface of a Ni foam. The Ni foam-supported Ni_2P nanosheet (Ni_2P NS/NF) electrode shows a remarkable specific capacitance of 2141 F g^{-1} at a scan rate of 50 mV s^{-1} and remains as high as 1109 F g^{-1} even at the current density of 83.3 A g^{-1}. The specific capacitance is much larger than those of $Ni(OH)_2$ NS/NF (747 F g^{-1} at 50 mV s^{-1}). Furthermore, the electrode retains a high specific capacitance of 1437 F g^{-1} even after 5000 cycles at a current density of 10 A g^{-1}, in sharp contrast with only 403 F g^{-1} of $Ni(OH)_2$ NS/NF at the same current density. The similar enhanced performance is observed for Ni_2P powder, which eliminates the influence of nickel foam. The enhanced supercapacitor performances are attributed to the 3D porous nanosheets network, enhanced conductivity, and two active components of Ni^{2+} and $P\delta^-$ with rich valences of Ni_2P.

1. Introduction

Supercapacitors or electrochemical capacitors have been hailed as promising electrochemical energy storage devices and drawn extensive interest due to their high power density, fast charging/discharging rate, and excellent cycle performance.[1] Supercapacitors may be used for hybrid electric vehicles, consumer electronics, and backup energy systems.[2] In recent years, great efforts have been dedicated to the development and engineering of new materials and structures for enhanced capacitance performance.[3] For instance, pseudocapacitors that store energy through reversible Faradaic reactions on the electrode surface, such as metal oxides[4] and hydroxides,[5] usually provide high specific capacitance. Nevertheless, these metal oxides or hydroxides are kinetically unfavorable for fast electron transport required for high power density.[6] As a comparison, transition metal phosphides possess the metalloid characteristics and superior electrical conductivity,[7] which have been used as anode materials for lithium-ion batteries,[8] hydrotreating catalysts,[9] electrocatalysts for the H_2 evolution,[10] etc. To the best of our knowledge, reports of transition metal phosphides as a cathode material for electrochemical capacitors have been scarce. This is the primary motivation of the present study in which we use a general and effective phosphorization approach to prepare various transition metals phosphide nanostructures and examined the capacitance performance of the hybrid electrodes.

Note that Ni foam has been used extensively as a supporting substrate for supercapacitor electrodes, due to the high conductivity and interconnected pores.[11] Electroactive materials of various morphologies, including nanoparticle,[12] nanowire,[13] and nanosheet,[14] have been deposited onto nickel foam to construct supercapacitor electrodes. In this study, 3D networks of Ni_2P nanosheets were grown on the surface of a Ni foam (Ni_2P NS/NF) by a phosphorization strategy from $Ni(OH)_2$ nanosheets. A variety of experimental techniques including transmission electron microscopy (TEM) and X-ray photoelectron spectroscopy (XPS) were used to characterize the resulting composite structures. The hybrid structure was then used directly as a capacitor electrode, and electrochemical studies showed an excellent specific capacitance of 2141 F g^{-1} at the potential scan rate of 50 mV s^{-1} and remained as high as 1109 F g^{-1} even at the current density of 83.3 A g^{-1} in a 6.0 M KOH aqueous electrolyte, much higher that of the as-synthesized $Ni(OH)_2$ nanosheet/Ni foam electrode. This is the best performance that has ever

K. Zhou, Dr. W. Zhou, L. Yang, J. Lu,
Dr. S. Cheng, Prof. Z. Tang, Prof. L. Li, Prof. S. Chen
New Energy Research Institute
School of Environment and Energy
South China University of Technology
Guangzhou Higher Education Mega Center
Guangzhou, Guangdong 510006, P.R. China
E-mail: eszhouwj@scut.edu.cn; shaowei@ucsc.edu
Prof. W. Mai
Department of Physics and Siyuan Laboratory
Jinan University
Guangzhou, Guangdong 510632, P.R.China
Prof. S. Chen
Department of Chemistry and Biochemistry
University of California
1156 High Street, Santa Cruz, CA 95064, USA

DOI: 10.1002/adfm.201503662

been reported with nickel-based materials in the literatures. An asymmetric supercapacitor was also fabricated with Ni_2P NS/NF as the positive electrode and activated carbon (AC) as the negative electrode. This asymmetric supercapacitor device was able to light a commercial red light-emitting diode (LED) array after charging at 1.6 V for 30 s, suggesting a great potential for practical applications. Moreover, the phosphorization treatment to enhance the pseudocapacitance of metal oxides or hydroxides (such as $Ni(OH)_2$, $Co(OH)_2$, MnO_2, and Fe_3O_4) has been demonstrated to be a general and effective strategy.

2. Result and Discussion

Figure 1a shows the X-ray diffraction (XRD) patterns of the Ni foam, $Ni(OH)_2$ NS/NF, and Ni_2P NS/NF. For the Ni foam substrate, three peaks are well defined at 2θ = 44.5°, 52.0°, and 76.4° which are consistent with the diffraction patterns of metallic nickel (JCPDS No. 04-0850). After hydrothermal treatment in the presence of $NiCl_2$ and hexamethylene tetramine (HMT), three additional peaks appeared at 11.4°, 33.4°, and 59.9°, which corresponded to the (003), (101), and (110) planes of α-phase $Ni(OH)_2 \cdot 0.75H_2O$ (JCPDS No. 38-0715),[15] respectively, confirming the formation of $Ni(OH)_2$ NS/NF hybrids. Note that these three peaks vanished after $Ni(OH)_2$ NS/NF reacted further with PH_3 produced by thermal decomposition of $NaH_2PO_2 \cdot H_2O$. However, three new peaks emerged at 40.9°, 47.6°, and 54.4° that matched well the diffractions of the (111), (210), and (300) crystalline planes of hexagonal Ni_2P (JCPDS No. 03-0953), signifying the successful conversion of $Ni(OH)_2$ to Ni_2P and hence the formation of Ni_2P NS/NF.

From the scanning electron microscope (SEM) image in Figure 1b, one can see that in contrast to the smooth surface of the pristine Ni foam (Figure 1b, inset), hydrothermal treatment led to the formation of a 3D grid structure of $Ni(OH)_2$ nanosheets on the Ni foam surface. At high magnification (Figure 1c) it can be seen that the $Ni(OH)_2$ nanosheets were densely interconnected with each other and grown uniformly on the Ni foam surface to form a multilevel structure. After phosphatized conversion from $Ni(OH)_2$ to hexagonal Ni_2P, the color of the Ni foam changed from light green to black (Figure S1, Supporting Information), while the overall morphology of the sample remained unchanged, as depicted in Figure 1d. However, it can be seen that the Ni_2P nanosheets were rather wrinkled (Figure 1e). Furthermore, The elements oxygen (probably from the superficial passivation of the Ni_2P nanosheets, a phenomenon also is seen for other metal phosphides,[16] nickel, and phosphorus were detected by energy dispersive X-ray (EDX) analysis. In addition, from the elemental mapping images (Figure 1f–h) one can see that the elements of Ni and

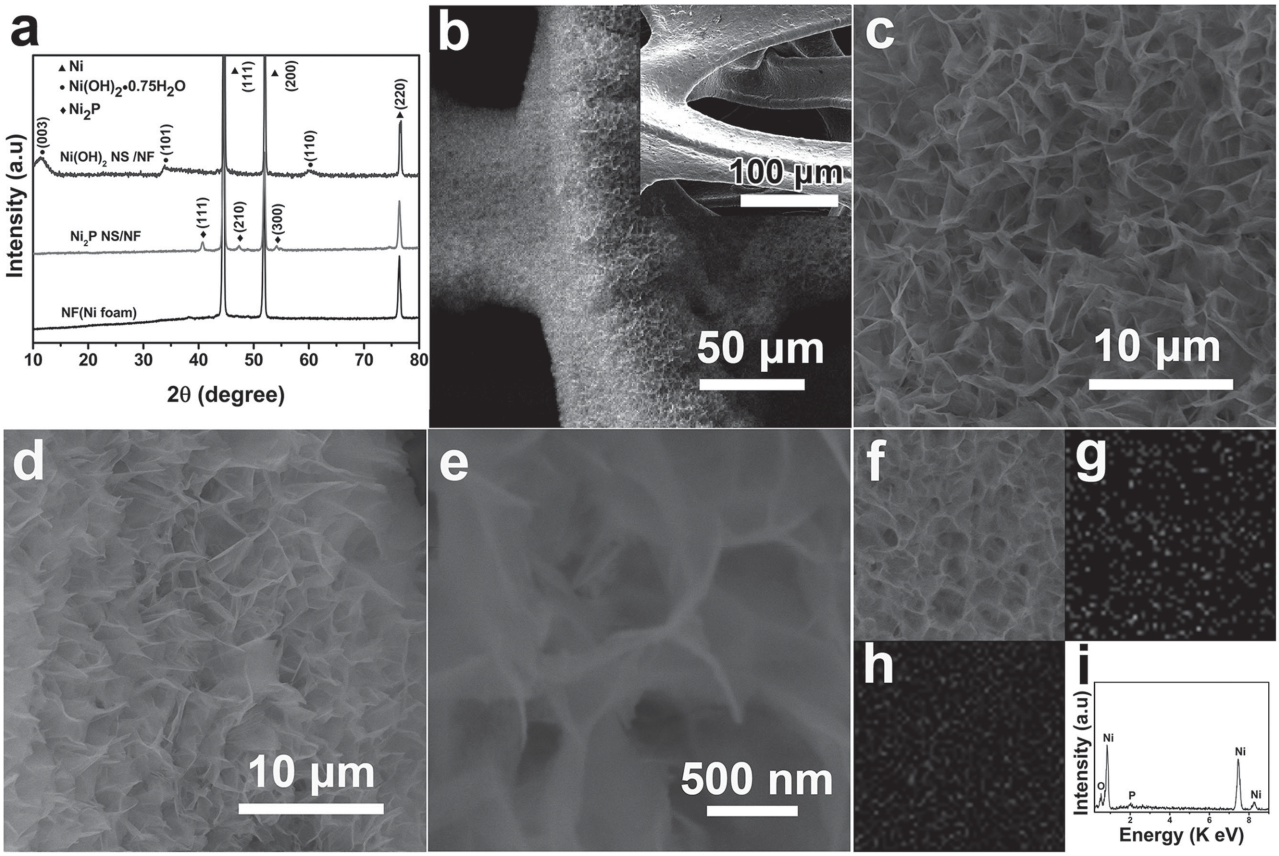

Figure 1. a) XRD patterns of Ni foam, $Ni(OH)_2$ NS/NF, and Ni_2P NS/NF. SEM images of b) Ni foam covered with $Ni(OH)_2$ nanosheets (inset is the Ni foam before nanosheet growth), c) $Ni(OH)_2$ NS/NF, and d,e) Ni_2P NS/NF. f) STEM image and the corresponding EDX elemental mapping images of g) element P and h) element Ni for Ni_2P NS/NF. i) EDX spectrum of Ni_2P NS/ NF.

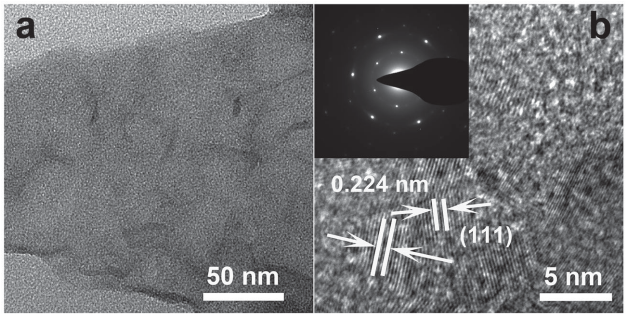

Figure 2. a) Low- and b) high-resolution TEM images of a Ni_2P nanosheet. The inset of (b) is the corresponding SAED pattern.

P were uniformly distributed throughout the entire nanosheet arrays. Taken together, these results indicate that the $Ni(OH)_2$ nanosheets on the Ni foam surface had been successfully converted to Ni_2P nanosheets via a phosphorization reaction.

Further structural details were revealed in high resolution transmission electron microscopy (HR)TEM analyses. From the low-resolution image in **Figure 2**a, one can clearly see wrinkling of the Ni_2P nanosheets that were detached from the Ni foam, consistent with SEM results in Figure 1e. From the high-resolution image in Figure 2b, it can be seen that the nanosheets were actually constituted of a large number of crystalline nanoparticles, and the well-defined lattice fringes showed an interplanar spacing of 0.224 nm, consistent with the (111) crystalline planes of hexagonal Ni_2P.[17] The corresponding selected area electron diffraction (SAED) pattern was depicted in the inset of Figure 2b, where the diffraction spots and rings corresponded to single-crystal nanoparticles and polycrystalline nanosheets, respectively, in good agreement with HRTEM results.

The valence states of Ni and P in the Ni_2P NS/NF and $Ni(OH)_2$ NS/NF hybrids were then investigated by XPS measurements. In **Figure 3**a, the peak centered at 129.8 eV may be assigned to $P^{\delta-}$ in the form of metal phosphide,[18] and the peak at 134.0 eV is typical of phosphate species, likely due to superficial passivation of phosphide particles.[18,19] From Figure 3b, one can see that for the $Ni(OH)_2$ NS/NF sample (bottom curve), the peak at 855.5 eV is consistent with the Ni $2p_{3/2}$ electrons of $Ni(OH)_2$.[20] After phosphorization reaction to form Ni_2P NS/NF, the peak centered at 853.5 eV may be assigned to $Ni^{\delta+}$ in Ni_2P,[18,21] and the one at 857.0 eV to Ni^{2+} most likely in the form of phosphate salts as a consequence of superficial passivation, as suggested in the P 2p XPS spectrum in panel (a).[21] The broad peak centered at 861.4 eV is the shakeup satellite peak of the divalent Ni^{2+} species.[21] In addition, the peak centered at 532.0 eV of O 1s XPS spectrum (Figure S2, Supporting Information) is related to oxygen in the P—O environments,[22] corresponding to above result of P 2p spectrum. But the characteristic peak of oxygen species in the NiO phase at 529.8 eV is not detected in the O 1s spectrum of the Ni_2P NS/NF.[23] XRD result of the Ni_2P NS/NF has not detected the corresponding diffraction peaks of NiO. These results confirm the formation of Ni_2P nanosheets without other crystal phase on the Ni foam surface.

Cyclic voltammetry (CV) and galvanostatic charging/discharging tests were then carried out to evaluate the electrochemical properties of Ni_2P NS/NF in an aqueous electrolyte of 6.0 M KOH in a three-electrode configuration. For comparison, the NiO NS/NF electrode was prepared by calcining the $Ni(OH)_2$ NS/NF at same condition without sodium hypophosphite. **Figure 4**a shows the CV curves of the Ni_2P NS/NF electrodes in the potential range of –0.1 to +0.5 V at the scan rate of 5 mV s^{-1} with a specific capacitance of 3708 F g^{-1}, which is much larger than those of $Ni(OH)_2$ NS/NF (1592 F g^{-1}) and NiO NS/NF electrode (1180 F g^{-1}). The results demonstrate that the excellent electrochemical performance mainly attributes to the Ni_2P nanosheets derived from the phosphorization treatment of $Ni(OH)_2$ nanosheets, not from NiO. In fact, there are no NiO in Ni_2P NS/NF electrodes, which were confirmed by XPS (Figure 3) and XRD (Figure 1a). In addition, in order to eliminate the influence of nickel foam on Ni_2P NS/NF, the CV of NF-P electrode (prepared by calcining the pure Ni foam in PH_3 atmosphere) was then carried out, which possessed the very small capacitance, which was similar with pure Ni foam (Figure S3, Supporting Information). Besides, in order to further verify the results, the Ni_2P powder was prepared by calcining the $Ni(OH)_2$ powder at same condition with sodium hypophosphite without Ni foam (Figure S4, Supporting Information). The Ni_2P powder possesses the much higher specific capacitance of 2138 F g^{-1} at 5 mV s^{-1} (904 F g^{-1} at 10 A g^{-1}) than that of $Ni(OH)_2$, which is 1331 F g^{-1} at 5 mV s^{-1} (564 F g^{-1} at 10 A g^{-1}) (Figure S5, Supporting Information). However, the specific surface of the Ni_2P powder is 13.4 m^2 g^{-1}, much smaller than 101.5 m^2 g^{-1} of $Ni(OH)_2$ powder (Figure S6, Supporting Information), which confirms that the enhanced performance is derived from the phosphorization treatment, not from electrical double-layer capacitor.

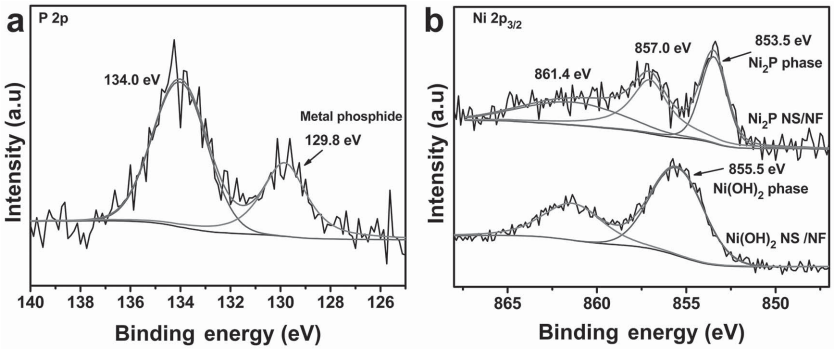

Figure 3. a) XPS spectrum of P 2p electrons of Ni_2P NS/NF. b) XPS spectra of Ni $2p_{3/2}$ electrons of (top curve) Ni_2P NS/NF and (bottom curve) $Ni(OH)_2$ NS/NF.

From these voltammetric measurements, the Ni_2P NS/NF electrode was found to exhibit a specific capacitance of 2141 F g^{-1} at 50 mV s^{-1} (Figure 4b,c), about three times larger than 747 F g^{-1} of $Ni(OH)_2$ NS/NF. Notably, even at 100 mV s^{-1} the specific capacitance of Ni_2P NS/NF remained as high as 1323 F g^{-1}. Figure 4d depicted the galvanostatic charging/discharging curves of the Ni_2P NS/NF electrode in 6.0 M KOH at different current densities. The corresponding specific capacitances were then calculated from the discharging

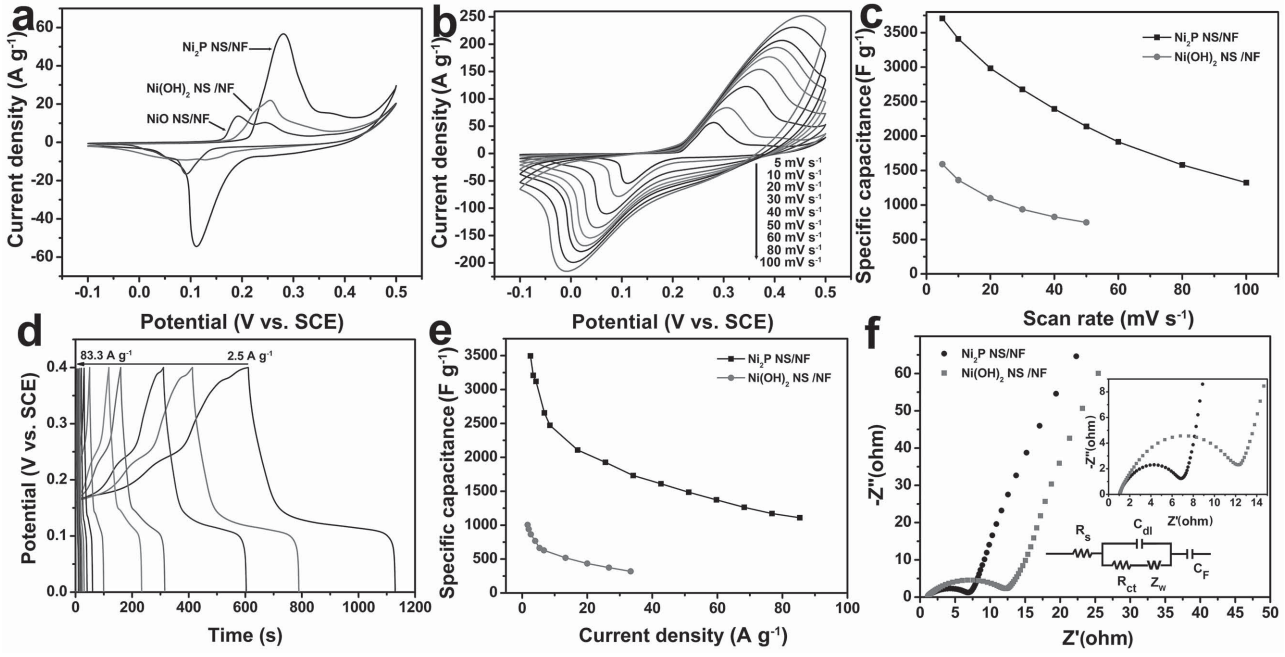

Figure 4. a) CV curves of Ni_2P NS/NF, $Ni(OH)_2$ NS/NF, and NiO NS/NF at the scan rate of 5 mV s^{-1} in 6.0 M KOH. b) CV curves of Ni_2P NS/NF at different scan rates. c) Specific capacitances of the $Ni(OH)_2$ NS/NF and Ni_2P NS/NF electrodes as a function of scan rate. d) Galvanostatic charge/discharge curves of the Ni_2P NS/NF electrode at different current densities. e) Specific capacitances of $Ni(OH)_2$ NS/NF and Ni_2P NS/NF as a function of current density. f) EIS plots of $Ni(OH)_2$ NS/NF and Ni_2P NS/NF (the inset shows the enlarged view of the high frequency region and the equivalent circuit diagram of different elements from the EIS analysis), where R_s is the equivalent series resistance, C_{dl} is a double layer capacitance, R_{ct} is the charge-transfer resistance, Z_w is a Warburg impedance, and C_F is a pseudocapacitance.

profiles and presented in Figure 4e, where a high specific capacitance (3496 F g^{-1}) was found at a discharge current density of 2.5 A g^{-1}, and even at 83.3 A g^{-1}, the specific capacitance of Ni_2P NS/NF remained at 1109 F g^{-1}. It can be seen that the Ni_2P NS/NF electrode exhibited much larger capacitance than $Ni(OH)_2$ NS/NF at the same current density (Figure 4e). This remarkable capacitance performance is drastically better than the leading results of relevant Ni-based materials ever reported in the recent literature, such as Ni-coated Ni_2P (1115 F g^{-1} at 2 A g^{-1}),[6b] Ni_2P/rGO (2266 F g^{-1} at 5 mV s^{-1}),[24] amorphous $Ni(OH)_2$ (3262 F g^{-1} at 5 mV s^{-1}),[25] Ni_3S_2@$Ni(OH)_2$/3DGN (1277 F g^{-1} at 2 mV s^{-1}),[26] and NiO-3D graphene (1829 F g^{-1} at 3 A g^{-1})[27] (see Table S1, Supporting Information, for a detailed comparison). Importantly, the Ni_2P NS/NF electrode in the present study also exhibited a high areal capacitance of 4.1 F cm^{-2} at 3 mA cm^{-2} and 1.3 F cm^{-2} at 100 mA cm^{-2} (Figure S7, Supporting Information).

To further study the ion and electron transport kinetics of the Ni_2P NS/NF and $Ni(OH)_2$ NS/NF electrodes, electrochemical impedance spectroscopy (EIS) measurements were then carried out. As shown in Figure 4f, the impedance spectra, characteristic of typical electrochemical capacitors, are composed of one semicircle and a linear segment in the high and low frequency region, respectively.[28] The impedance spectra of the Ni_2P NS/NF and $Ni(OH)_2$ NS/NF electrodes might both be fitted to the same equivalent circuit (inset of Figure 4f). The intercept at the real axis represents the equivalent series resistance (R_s), which is a combination of ionic resistance of the electrolytes, electronic resistance of the electrode materials, and interface resistance.[29] R_s of the Ni_2P NS/NF electrode was estimated to be around 1.0 Ω, somewhat lower than that (1.2 Ω) of $Ni(OH)_2$ NS/NF, indicating low internal resistance of both electrodes. R_{ct} for the redox reactions at the electrode/electrolyte interface can be defined by the diameter of the semicircle,[30] and R_{ct} for Ni_2P NS/NF (4.1 Ω) was found to be lower than that of $Ni(OH)_2$ NS/NF (7.8 Ω), consistent with the voltammetric results presented in Figure 4a. This might be ascribed to the higher conductivity of Ni_2P (8.6×10^{-4} Ω cm) [31] than that of $Ni(OH)_2$ (10^{-1} Ω cm).[32] This was conducive to faster charge transfer within the electrode and at the electrode/electrolyte interface. Furthermore, the Warburg impedance was also lower for Ni_2P NS/NF than $Ni(OH)_2$ NS/NF electrode; yet the parallelism of the two linear segments implies similar ion diffusion dynamics at the two electrodes as both consisted of a 3D interconnected porous network.[33]

The electrochemical stability of the Ni_2P NS/NF and $Ni(OH)_2$ NS/NF electrodes was then investigated by galvanostatic charge/discharge measurements at a current density of 10 A g^{-1}. As shown in **Figure 5**a, the two electrodes exhibited a similar changing trend of the specific capacitance. The increase of the specific capacitances in early cycles may be ascribed to the repetitive charging/discharging cycles that improved ion accessibility in the electrodes, which has been reported previously.[28,34] Note that from XPS measurements of the Ni_2P NS/NF electrode after the cycle tests (Figure 5b), the Ni 2p peak of Ni_2P (853.5 eV) remained well defined. However, the binding energy of the Ni^{2+} ions shifted to 856.5 eV from 857.0 eV corresponding to $Ni(OH)_2$. A similar result can been seen from the corresponding SAED pattern (Figure S8, Supporting Information), where the diffraction rings corresponded to polycrystalline $Ni(OH)_2$. So, the diminishment of the capacitance performance after 2000 cycles may be ascribed to the formation of $Ni(OH)_2$ from the surface of Ni_2P via reacting with the

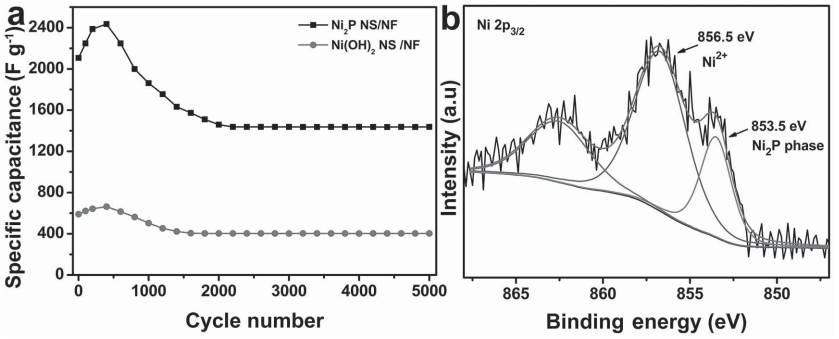

Figure 5. a) Cycling stability of the Ni_2P NS/NF and $Ni(OH)_2$ NS/NF at a current density of 10 A g^{-1}. b) XPS survey spectrum of Ni $2p_{3/2}$ of the Ni_2P NS/NF after the cycle test.

electrolyte. Nevertheless, the specific capacitance remained almost steady at 1437 F g^{-1} from 2000 to 5000 charging/discharging cycles (Figure 5a), in sharp contrast with $Ni(OH)_2$ NS/NF where the specific capacitance was more than three times lower at only 403 F g^{-1} at the same current density. Furthermore, the Ni_2P NS/NF electrode maintained the nanosheet structures after 5000 cycle tests (Figure S9, Supporting Information). Therefore, we think that so, the phosphorization treatment increases the capacitance value and improves the cycle stability after charge/discharge.

Take into all above results and analysis, this remarkable supercapacitor performance of the Ni_2P NS/NF electrode might be accounted for by the following factors: (i) the 3D interconnected networks of porous nanosheets provided sufficient space to facilitate ion diffusion; (ii) Ni_2P with the enhanced conductivity would facilitate electron transfer within the electrode and at the electrode/electrolyte interface; (iii) two active components of Ni^{2+} and $P^{\delta-}$ with rich valences in Ni_2P involved in electron transfer reaction and offered abundant active sites for redox reactions to enhance thepseudocapacitance; (iv) the $Ni(OH)_2$ on Ni_2P after 2000 cycles ensured the good cycle stability. A similar conversion from metal nitride or sulfide into the core–shell structure of metal nitride or sulfide @ hydroxide has been reported.[35]

In order to further evaluate the Ni_2P NS/NF electrode for practical applications, an asymmetric supercapacitor device encapsulated in a button battery was fabricated using the Ni_2P NS/NF electrode as the cathode and AC on a Ni foam as the anode in 6 M KOH with one piece of cellulose paper as the separator. In addition, the surface of the positive electrode was coating with a PVA/KOH gel electrolyte to increase cycle stability of the Ni_2P NS/NF electrode.[36] According to the CVs of the individual electrodes acquired in a separate three-electrode cell (Figure S10, Supporting Information), the ideal mass ratio of the positive electrode to the negative electrode was estimated to be 0.11 to balance their charges. A series of CV plots of the asymmetric supercapacitor at different potential windows at 50 mV s^{-1} are shown in **Figure 6**a. One can see that

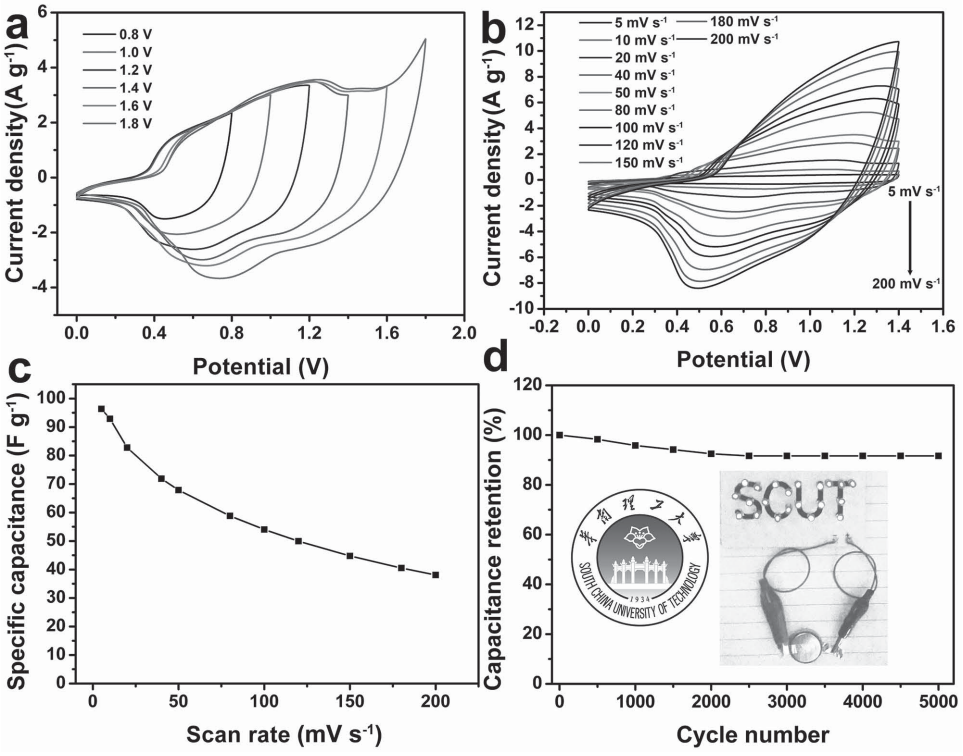

Figure 6. Electrochemical characterization of the Ni_2P NS/NF//AC asymmetric supercapacitor device: a) CV curves collected in different scan voltage windows at the scan rate of 50 mV s^{-1}. b) CV curves at different scan rates with a voltage window of 0–1.4 V. c) Specific capacitances of the device as a function of scan rate. d) Cycling stability of the device at a current density of 1.0 A g^{-1} (inset: LEDs array powered by the asymmetric supercapacitor device).

a pair of broad voltammetric peaks appeared between +0.4 and +1.4 V, most likely arising from faradaic reactions of Ni_2P, similar to the behaviors observed when the electrode was immersed in a liquid electrolyte solution (Figure 4). Note that the voltammetric features appeared to involve multiple peaks with the gradual expansion of the potential window, suggesting varied energetic states of Ni_2P in solid state. At potentials beyond +1.6 V, oxygen evolution started to occur. Thus, 1.4 V was determined to be the working potential window. Figure 6b shows the CV curves of the asymmetric supercapacitor at potential scan rates ranging from 5 to 200 mV s^{-1} within the potential window of 0–1.4 V. All curves exhibited a similar shape, except that the peak splitting increased with increasing potential scan rate. The specific capacitance as a function of scan rate is plotted in Figure 6c. Note that the specific capacitance calculated from the CV curves was based on the total mass of the active materials of the two electrodes. It can be seen that the specific capacitance of the asymmetric supercapacitor is 96 F g^{-1} at the scan rate of 5 mV s^{-1}, and 38F g^{-1} at 200 mV s^{-1}. It should be noted that the specific capacitance of the Ni_2P electrode (2141 F g^{-1} at 50 mV s^{-1}) was drastically higher than that (184 F g^{-1}) of the AC counter electrode, resulting in a suppressed performance of the full device. The galvanostatic charge/discharge curves of the full device are depicted in Figure S11a (Supporting Information), and the specific capacitance calculated by the discharging profile was 62 F g^{-1} at the discharge current density of 0.5 A g^{-1} (Figure S11b, Supporting Information). The impedance spectra of the device are similar to those observed with the single electrode, composed of one semicircle in the high frequency region and a linear segment at low frequencies (Figure S11c, Supporting Information).[37]

The asymmetric supercapacitor device also shown the good electrochemical stability, that 91.3% of the device capacitance was retained even after 5000 charging/discharging cycles (Figure 6d). Furthermore, as depicted in the inset of Figure 6d, one can see that a single device could light a commercial red LED array after being charged at 1.6 V for 30 s. Based on the CV data, the Ragone plots of the Ni_2P NS/NF// AC asymmetric supercapacitor are displayed in Figure S11d (Supporting Information), where one can see that an energy density of 26 W h kg^{-1} can be achieved at a power density of 337 W kg^{-1} and still reaches 10 W h kg^{-1} even when the power density increases to 5332 W kg^{-1}.

To verify the universality of the phosphorization treatment to enhance the pseudocapacitance of synthesized metal oxides or hydroxides, we extended the strategy to Co(OH)F/NF, MnO_2/NF, and Fe_2O_3 powder. **Figure 7**a shows the XRD patterns of the cobalt hydroxide precursor obtained under a hydrothermal process. The diffraction peaks for the Co precursor at 20.9°, 33.5°, 35.6°, and 38.8° can be well ascribed to the (110), (201), (111), and (211) planes of the Co(OH)F (JCPDS No. 50-0827),[38] respectively. After phosphorization treatment in the presence of $NaH_2PO_2 \cdot H_2O$ at 300 °C, new peaks emerged at 40.7°, 41.0°, 43.3°, and 48.7° that matched well the diffractions of the (121),

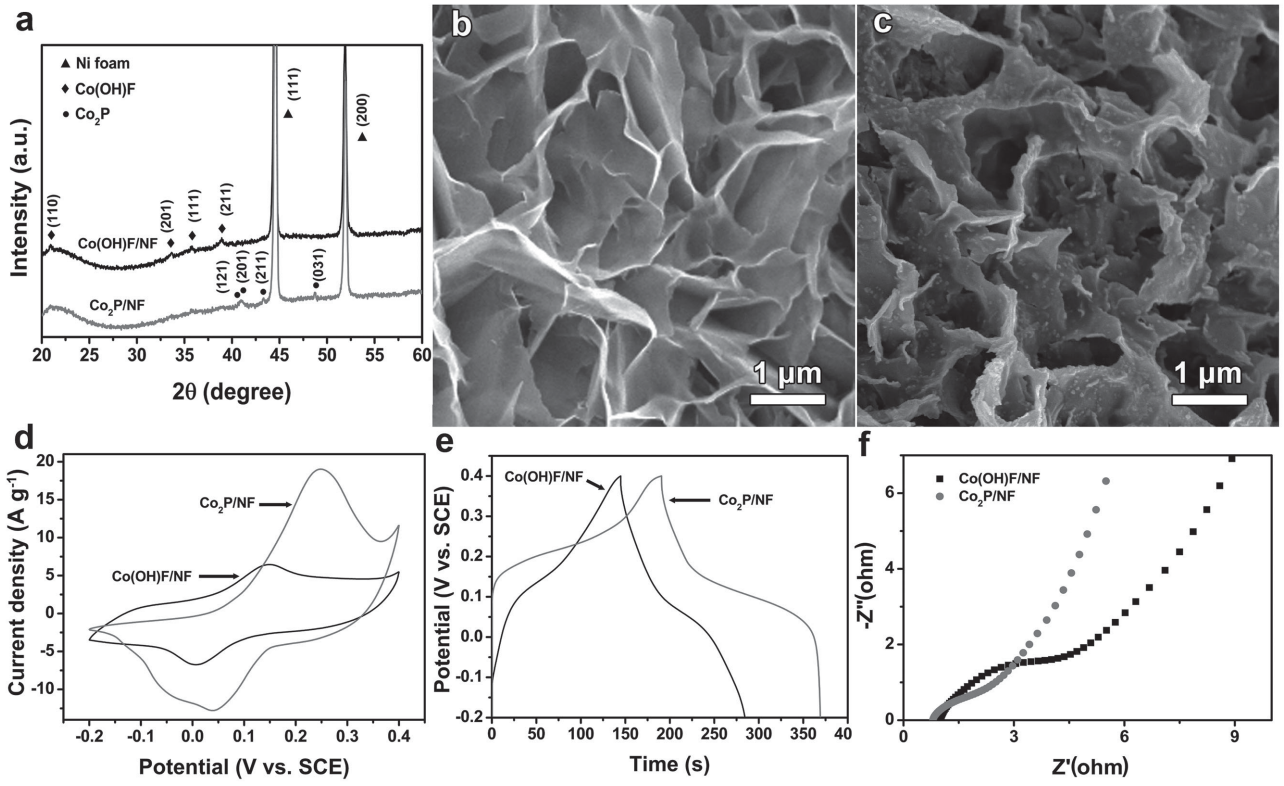

Figure 7. a) XRD patterns of Co(OH)F/NF and Co_2P/NF. SEM images of b) Co(OH)F/NF and c) Co_2P/NF. d) CV curves of Co(OH)F/NF and Co_2P/NF at the scan rate of 5 mV s^{-1} in 6.0 M KOH. e) Galvanostatic charge/discharge curves of the Co(OH)F/NF and Co_2P/NF at the current density of 10 mA cm^{-2} in 6.0 M KOH. f) EIS plots of Co(OH)F/NF and Co_2P/NF in 6.0 M KOH.

(201), (211), and (031) crystalline planes of Co_2P (JCPDS No. 32-0306),[16a] suggesting the successful conversion of Co(OH)F to Co_2P. XPS results also demonstrate the successful synthesis of Co_2P (Figure S12, Supporting Information). The Co(OH)F nanosheet arrays with a network structure were grown uniformly on the Ni foam surface (Figure 7b). After phosphatized conversion to Co_2P, the network architecture was well maintained, but the surface of the obtained Co_2P nanosheets becomes rougher (Figure 7c). CV and galvanostatic charging/discharging tests were then carried out to compare the electrochemical properties of Co_2P/NF and Co(OH)F/NF in an aqueous electrolyte of 6.0 M KOH under the same conditions. Figure 7d shows the Co_2P/NF electrode (gray curve) exhibited a more lager redox couple than Co(OH)F/NF, accompanying with lager CV curve area. The specific capacitance of Co_2P/NF is 2193 F g^{-1} at 5 mV s^{-1} calculated from CV curve, almost twice larger than 1222 F g^{-1} of Co(OH)F/NF. As the galvanostatic charging/discharging curves shown in Figure 7e, the Co_2P/NF electrode exhibits a longer discharging time than Co(OH)F/NF at the same current density of 10 mA cm^{-2}. The corresponding specific capacitance of Co_2P/NF is 1189 F g^{-1} at 10 mA cm^{-2}, higher than 698 F g^{-1} of Co(OH)F/NF. Moreover, as shown in Figure 7f, the impedance spectra of the electrodes show the characteristic of typical electrochemical capacitors as similar to the impedance spectra of Ni_2P NS/NF and $Ni(OH)_2$ NS/NF discussed above. The diameter of the semicircle in the high frequency region of the Co_2P/NF electrode is smaller than that of Co(OH)F/NF, indicting a lower charge-transfer resistance at the electrode/electrolyte interface for Co_2P/NF, which is beneficial for the supercapacitor performance. In all, after the Co(OH)F nanosheet arrays on the Ni foam surface were converted to Co_2P nanosheet arrays by a phosphorization reaction, the supercapacitor performance can markedly be improved. A similar phenomenon of the enhanced supercapacitor performance by a phosphorization reaction is observed for MnO_2/NF and Fe_2O_3, as shown in Figures S13–S15 (Supporting Information), which confirms the generality of this phosphorization strategy.

3. Conclusions

In summary, 3D interconnected networks of Ni_2P nanosheets were grown on the surface of Ni foam via a phosphorization reaction of $Ni(OH)_2$ nanosheets that were prepared by a hydrothermal process. The resulting Ni_2P NS/NF hybrid electrode was found to exhibit a remarkable specific capacitance of 2141 F g^{-1} at the potential scan rate of 50 mV s^{-1} in a 6.0 M KOH aqueous solution, about three times higher than that of $Ni(OH)_2$ NS/NF (747 F g^{-1}). Note that this is higher than leading results of relevant Ni-based supercapacitor electrodes ever reported in the literatures. In addition, the Ni_2P NS/NF electrode was found to retain a high specific capacitance of 1437 F g^{-1} even after 5000 charging and discharging cycles at a current density of 10 A g^{-1}. Furthermore, an asymmetric supercapacitor device based on the Ni_2P NS/NF hybrid and AC was observed to achieve a specific capacitance of 96 F g^{-1} at the scan rate of 5 mV s^{-1} with a stable operational voltage of 1.4 V and a maximum energy density of 26 W h kg^{-1}. What's more, the phosphorization strategy to enhance supercapacitor performance is general, simple, and effective, which can be extended to various kinds of transition metals, such as nickel, cobalt, manganese, and iron.

4. Experimental Section

Materials: Nickel chloride hexahydrate ($NiCl_2{\cdot}6H_2O$), cobalt nitrate hexahydrate ($Co(NO)_2{\cdot}6H_2O$), ferric chloride hexahydrate ($FeCl_3{\cdot}6H_2O$), potassium permanganate ($KMnO_4$), HMT, ammonium fluoride (NH_4F), urea ($CO(NH_2)_2$), and sodium hypophosphite ($NaH_2PO_2{\cdot}H_2O$) were purchased from Sinopharm Chemical Reagents Co., Ltd. All reagents were of analytical grade and used without further purification. Deionized water (DI water) was supplied with a Barnstead Nanopure Water System (18.3 MΩ cm).

Synthesis of Ni Foam Supported $Ni(OH)_2$ Nanosheets ($Ni(OH)_2$ NS/NF): Prior to the synthesis, a Ni foam was immersed in a HCl solution (1 M) in an ultrasound bath for 30 min to remove the oxide layer on the surface, and washed thoroughly with deionized water and absolute ethanol. The Ni Foam was then subject to a hydrothermal process to grow $Ni(OH)_2$ nanosheets ($Ni(OH)_2$ NS/NF) on the surface. In a typical procedure, $NiCl_2{\cdot}6H_2O$ (0.12 g) and HMT (0.4 g) were dissolved in DI water (20 mL) to form a pink solution. The solution was transferred to a 25 mL Teflon-lined stainless autoclave. A piece of the pretreated Ni foam was put in the autoclave. The autoclave was then sealed and heated at 100 °C for 10 h. After it was cooled down to room temperature, the Ni foam was washed with DI water and ethanol several times and dried in air. The weight of $Ni(OH)_2$ nanosheets was about 1.5 mg per 1 cm × 1 cm of the Ni foam by subtracting the weight before deposition from the weight after deposition.

Synthesis of Ni Foam Supported Ni_2P Nanosheets (Ni_2P NS/NF): The synthesis of Ni_2P NS/NF was carried out in a closed porcelain crucible placed at the middle of a horizontal tube furnace.[10a] $NaH_2PO_2{\cdot}H_2O$ powders (6.0 mg) were placed at the upstream side of the porcelain crucible and the as-grown $Ni(OH)_2$ NS/NF at the opposite end. The samples were heated to 300 °C at a heating rate of 5 °C min^{-1} for 2 h under an Ar flow. Ni_2P NS/NF was collected after the furnace was cooled to ambient temperature. The mass of the Ni_2P nanosheets on Ni foam was determined by subtracting the weight of Ni foam from the weight of the Ni_2P NS/NF. On average, 1.2 mg of Ni_2P nanosheets was grown on a 1 cm × 1 cm piece of Ni foam, as quantified by a high precision microbalance.

Synthesis of Ni Foam Supported NiO Nanosheets (NiO NS/NF): The as-prepared $Ni(OH)_2$ NS /NF was heated to 300 °C at a heating rate of 5 °C min^{-1} for 2 h under an Ar flow. After it was cooled down to room temperature, the Ni foam was washed with DI water and ethanol several times and dried in air. The weight of NiO nanosheets was about 1.2 mg per 1 cm × 1 cm of the Ni foam by subtracting the weight before deposition from the weight after deposition.

Phosphorization of Ni Foam (NF-P): The Ni foam was heated to 300 °C at a heating rate of 5 °C min^{-1} for 2 h under an Ar flow with $NaH_2PO_2{\cdot}H_2O$ powders (6.0 mg).

Structural Characterizations: The microstructural and morphological details of the samples were examined with a field-emission SEM (NOVA NANOSEM 430, FEI) and a Tecnai G220, FEI transmission electron microscope (TEM) at an acceleration voltage of 200 kV. Chemical compositions were evaluated by EDX spectroscopic measurements and element mapping (Philips Tecnai F20) and XPS (PHI X-tool) measurements. XRD analysis was performed on a Bruker D8 Advance powder X-ray diffractometer with Cu Kα (λ = 0.15406 nm) radiation. The surface area was characterized by Micromeritics ASAP 2010 with nitrogen adsorption at 77 K.

Electrochemical Measurements: All electrochemical measurements were carried out using a CHI 660E Electrochemical Workstation (CH Instruments, China) in a three-electrode configuration. The Ni_2P NS/NF hybrids were used directly as the working electrode, along with a

saturated calomel reference electrode (Hg/Hg_2Cl_2 in saturated KCl) and a Pt counter electrode. EIS measurements were then carried out in the frequency range from 0.01 Hz to 100 kHz. As for powder samples, 4 mg of the as-prepared samples and 1 mg acetylene black were dispersed into ethanol (1.9 mL) along with Nafion (0.1 mL, 5%). 5 µL of the obtained suspension was then dropcast onto a glassy carbon electrode by using a Hamilton microliter syringe, dried at ambient temperature, and used as the working electrode.

The asymmetric supercapacitor was fabricated with the Ni_2P NS/NF hybrid as the positive electrode and an AC as the negative electrode.[39] The negative electrode was prepared by mixing AC in ethanol with Nafion (5%), which was then coated onto a 1.5 cm × 1.5 cm Ni foam and dried at 100 °C. The polymer electrolyte was prepared by dissolving PVA (2 g) and KOH (3 g) in water (20 mL) at 95 °C under vigorous stirring until the solution became clear. The Ni_2P NS/NF electrode was coated with the PVA/KOH gel electrolyte as the positive electrode. The Ni_2P NS/NF positive electrode and the AC negative electrode were pressed individually with one piece of cellulose paper as the separator, and encapsulated in a button battery to form an asymmetric supercapacitor device with 6 M KOH as the electrolyte.

Calculations: Specific capacitances (F g^{-1}) were calculated from the CV (C_{m1}) and charge–discharge curves (C_{m2}) by Equations (1) and (2), respectively, where I_1 (A) is the response current, ΔV (V) is the voltage window, v (V s^{-1}) is the scan rate, I_2 (A) is the constant discharge current, Δt (s) is the discharging time, and m (g) is the weight of active materials. For the three-electrode configuration, m (g) is the weight of active materials for the single electrode. For the asymmetrical supercapacitor, m (g) is the total mass of active materials of the positive and negative electrodes

$$C_{m1} = \frac{\int I_1 dV}{vm\Delta V} \quad (1)$$

$$C_{m2} = \frac{I_2 \Delta t}{m\Delta V} \quad (2)$$

Areal capacitances (F cm^{-2}) were calculated from CV (C_{S1}) and charge–discharge curves (C_{S2}) by Equations (3) and (4), respectively, where S (cm^2) is the geometrical area of the electrode

$$C_{S1} = \frac{\int I_1 dV}{vS\Delta V} \quad (3)$$

$$C_{S2} = \frac{I_2 \Delta t}{S\Delta V} \quad (4)$$

Energy density (E) and power density (P) of the asymmetrical supercapacitor device were calculated from the CV curves at different scan rates by Equations (5) and (6), respectively, where t (s) is the time for a scan segment

$$E = \frac{1}{2} C_{m1} (\Delta V)^2 \quad (5)$$

$$P = \frac{E}{t} \quad (6)$$

Supporting Information

Supporting Information is available from the Wiley Online Library or from the author.

Acknowledgements

This work was supported by the National Recruitment Program of Global Experts, Zhujiang New Stars of Science & Technology (2014J2200061), Project of Public Interest Research and Capacity Building of Guangdong Province (2014A010106005), and the National Natural Science Foundation of China (51502096).

Received: August 29, 2015
Revised: October 3, 2015
Published online: November 10, 2015

[1] a) G. Wang, L. Zhang, J. Zhang, *Chem. Soc. Rev.* **2012**, *41*, 797; b) P. Simon, Y. Gogotsi, *Nat. Mater.* **2008**, *7*, 845; c) Z. Yu, L. Tetard, L. Zhai, J. Thomas, *Energy Environ. Sci.* **2015**, *8*, 702; d) L. L. Zhang, X. S. Zhao, *Chem. Soc. Rev.* **2009**, *38*, 2520.

[2] a) Y. Gogotsi, *Nature* **2014**, *509*, 568; b) J. R. Miller, P. Simon, *Science* **2008**, *321*, 651; c) X. Xu, S. Li, H. Zhang, Y. Shen, S. M. Zakeeruddin, M. Graetzel, Y.-B. Cheng, M. Wang, *ACS Nano* **2015**, *9*, 1782.

[3] a) S. Chen, W. Xing, J. Duan, X. Hu, S. Z. Qiao, *J. Mater. Chem. A* **2013**, *1*, 2941; b) B. L. Ellis, P. Knauth, T. Djenizian, *Adv. Mater.* **2014**, *26*, 3368.

[4] a) K. Zhou, W. Zhou, X. Liu, Y. Sang, S. Ji, W. Li, J. Lu, L. Li, W. Niu, H. Liu, S. Chen, *Nano Energy* **2015**, *12*, 510; b) Q. Lu, M. W. Lattanzi, Y. Chen, X. Kou, W. Li, X. Fan, K. M. Unruh, J. G. Chen, J. Q. Xiao, *Angew. Chem. Int. Ed.* **2011**, *50*, 6847.

[5] X. Dong, Z. Guo, Y. Song, M. Hou, J. Wang, Y. Wang, Y. Xia, *Adv. Funct. Mater.* **2014**, *24*, 3405.

[6] a) X. H. Xia, J. P. Tu, Y. Q. Zhang, Y. J. Mai, X. L. Wang, C. D. Gu, X. B. Zhao, *J. Phys. Chem. C* **2011**, *115*, 22662; b) Y. Lu, J.-k. Liu, X.-y. Liu, S. Huang, T.-q. Wang, X.-l. Wang, C.-d. Gu, J.-p. Tu, S. X. Mao, *CrystEngComm* **2013**, *15*, 7071.

[7] S. Carenco, D. Portehault, C. Boissière, N. Mézailles, C. Sanchez, *Chem. Rev.* **2013**, *113*, 7981.

[8] a) Y. Lu, J.-P. Tu, Q.-Q. Xiong, J.-Y. Xiang, Y.-J. Mai, J. Zhang, Y.-Q. Qiao, X.-L. Wang, C.-D. Gu, S. X. Mao, *Adv. Funct. Mater.* **2012**, *22*, 3927; b) D. Yang, Z. Lu, X. Rui, X. Huang, H. Li, J. Zhu, W. Zhang, Y. Lam, H. Hng, H. Zhang, Q. Yan, *Angew. Chem. Int. Ed.* **2014**, *53*, 9506.

[9] T. I. Korányi, Z. Vít, D. G. Poduval, R. Ryoo, H. S. Kim, E. J. M. Hensen, *J. Catal.* **2008**, *253*, 119.

[10] a) P. Jiang, Q. Liu, X. Sun, *Nanoscale* **2014**, *6*, 13440; b) J. Tian, Q. Liu, A. M. Asiri, X. Sun, *J. Am. Chem. Soc.* **2014**, *136*, 7587.

[11] a) H. Chen, L. Hu, M. Chen, Y. Yan, L. Wu, *Adv. Funct. Mater.* **2014**, *24*, 934; b) C. Guan, J. Liu, C. Cheng, H. Li, X. Li, W. Zhou, H. Zhang, H. J. Fan, *Energy Environ. Sci.* **2011**, *4*, 4496.

[12] Y. Ko, D. Shin, B. Koo, S. Woo Lee, W.-S. Yoon, J. Cho, *Nano Energy* **2015**, *12*, 612.

[13] a) W. Zhou, X. Liu, Y. Sang, Z. Zhao, K. Zhou, H. Liu, S. Chen, *ACS Appl. Mater. Interfaces* **2014**, *6*, 4578; b) Q. Wang, X. Wang, B. Liu, G. Yu, X. Hou, D. Chen, G. Shen, *J. Mater. Chem. A* **2013**, *1*, 2468.

[14] a) C. Yuan, J. Li, L. Hou, X. Zhang, L. Shen, X. W. Lou, *Adv. Funct. Mater.* **2012**, *22*, 4592; b) L. Qu, Y. Zhao, A. M. Khan, C. Han, K. M. Hercule, M. Yan, X. Liu, W. Chen, D. Wang, Z. Cai, W. Xu, K. Zhao, X. Zheng, L. Mai, *Nano Lett.* **2015**, *15*, 2037; c) X. Cao, Y. Shi, W. Shi, G. Lu, X. Huang, Q. Yan, Q. Zhang, H. Zhang, *Small* **2011**, *22*, 3163.

[15] X. Ma, J. Liu, C. Liang, X. Gong, R. Che, *J. Mater. Chem. A* **2014**, *2*, 12692.

[16] a) Z. Huang, Z. Chen, Z. Chen, C. Lv, M. G. Humphrey, C. Zhang, *Nano Energy* **2014**, *9*, 373; b) A. Han, H. Chen, Z. Sun, J. Xu, P. Du, *Chem. Commun.* **2015**, *51*, 11626.

[17] J. Park, B. Koo, K. Y. Yoon, Y. Hwang, M. Kang, J.-G. Park, T. Hyeon, *J. Am. Chem. Soc.* **2005**, *127*, 8433.

[18] Y. Shi, Y. Xu, S. Zhuo, J. Zhang, B. Zhang, *ACS Appl. Mater. Interfaces* **2015**, *7*, 2376.

[19] J. A. Cecilia, A. Infantes-Molina, E. Rodríguez-Castellón, A. Jiménez-López, *J. Catal.* **2009**, *263*, 4.
[20] D. P. Dubal, G. S. Gund, C. D. Lokhande, R. Holze, *ACS Appl. Mater. Interfaces* **2013**, *5*, 2446.
[21] J. A. Cecilia, A. Infantes-Molina, E. Rodríguez-Castellón, A. Jiménez-López, *J. Phys. Chem. C* **2009**, *113*, 17032.
[22] Y. Huang, D. Wu, J. Jiang, Y. Mai, F. Zhang, H. Pan, X. Feng, *Nano Energy* **2015**, *12*, 287.
[23] S. I. Kim, J. S. Lee, H. J. Ahn, H. K. Song, J. H. Jang, *ACS Appl. Mater. Interfaces* **2013**, *5*, 1596.
[24] C. An, Y. Wang, Y. Wang, G. Liu, L. Li, F. Qiu, Y. Xu, L. Jiao, H. Yuan, *RSC Adv.* **2013**, *3*, 4628.
[25] W. Jiang, D. Yu, Q. Zhang, K. Goh, L. Wei, Y. Yong, R. Jiang, J. Wei, Y. Chen, *Adv. Funct. Mater.* **2015**, *25*, 1063.
[26] W. Zhou, X. Cao, Z. Zeng, W. Shi, Y. Zhu, Q. Yan, H. Liu, J. Wang, H. Zhang, *Energy Environ. Sci.* **2013**, *6*, 2216.
[27] C. Wang, J. Xu, M.-F. Yuen, J. Zhang, Y. Li, X. Chen, W. Zhang, *Adv. Funct. Mater.* **2014**, *24*, 6372.
[28] J. Ji, L. L. Zhang, H. Ji, Y. Li, X. Zhao, X. Bai, X. Fan, F. Zhang, R. S. Ruoff, *ACS Nano* **2013**, *7*, 6237.
[29] Y. Yang, L. Li, G. Ruan, H. Fei, C. Xiang, X. Fan, J. M. Tour, *ACS Nano* **2014**, *8*, 9622.
[30] T. Zhai, X. Lu, Y. Ling, M. Yu, G. Wang, T. Liu, C. Liang, Y. Tong, Y. Li, *Adv. Mater.* **2014**, *26*, 5869.
[31] A. Panneerselvam, M. A. Malik, M. Afzaal, P. O'Brien, M. Helliwell, *J. Am. Chem. Soc.* **2008**, *130*, 2420.
[32] X. Wang, J. Yan, H. Yuan, Z. Zhou, D. Song, Y. Zhang, L. Zhu, *J. Power Sources* **1998**, *72*, 221.
[33] L. L. Zhang, X. Zhao, M. D. Stoller, Y. Zhu, H. Ji, S. Murali, Y. Wu, S. Perales, B. Clevenger, R. S. Ruoff, *Nano Lett.* **2012**, *12*, 1806.
[34] a) X. Lu, D. Zheng, T. Zhai, Z. Liu, Y. Huang, S. Xie, Y. Tong, *Energy Environ. Sci.* **2011**, *4*, 2915; b) X. H. Xia, J. P. Tu, Y. J. Mai, X. L. Wang, C. D. Gu, X. B. Zhao, *J. Mater. Chem.* **2011**, *21*, 9319.
[35] a) K. Xu, P. Chen, X. Li, Y. Tong, H. Ding, X. Wu, W. Chu, Z. Peng, C. Wu, Y. Xie, *J. Am. Chem. Soc.* **2015**, *137*, 4119; b) L. Hou, C. Yuan, D. Li, L. Yang, L. Shen, F. Zhang, X. Zhang, *Electrochim. Acta* **2011**, *56*, 7454.
[36] a) X. Lu, G. Wang, T. Zhai, M. Yu, S. Xie, Y. Ling, C. Liang, Y. Tong, Y. Li, *Nano Lett.* **2012**, *12*, 5376; b) X. Lu, M. Yu, T. Zhai, G. Wang, S. Xie, T. Liu, C. Liang, Y. Tong, Y. Li, *Nano Lett.* **2013**, *13*, 2628.
[37] Z. Fan, J. Yan, T. Wei, L. Zhi, G. Ning, T. Li, F. Wei, *Adv. Funct. Mater.* **2011**, *21*, 2366.
[38] W. Mei, J. Huang, L. Zhu, Z. Ye, Y. Mai, J. Tu, *J. Mater. Chem.* **2012**, *22*, 9315.
[39] K. Zhou, W. Zhou, Y. Du, X. Liu, Y. Sang, W. Li, J. Lu, H. Liu, S. Chen, *Sci. Adv. Mater.* **2015**, *7*, 571.